*Astronomy & Astrophysics* manuscript no. output
March 9, 2020


# MEGARA, the intermediate-resolution optical IFU and MOS of GTC

A. Gil de Paz[1], J. Gallego[1], E. Carrasco[2], J. Iglesias[3], R. Cedazo[4], M. García Vargas[5], J. Vílchez[3], N. Cardiel[1], A. Castillo-Morales[1], P. Gómez-Cambronero[5], I. Martínez-Delgado[5], S. Pascual[1], A. Pérez-Calpena[5], A. Sánchez-Penim[1], J. Carbajo-Hijarrubia[1], P. Andrés[1], X. Arrillaga[6], J. Avilés[3], J. Bonache[1], A. Bouquin[1], M. Carrera[6], E. Castillo[2], J. Dormido[1], C. Eliche Moral[1], S. Esteban[1], D. Ferrusca[2], E. González[4], B. Lefort[5], J.A. López[1], M. Maldonado[5], R. Marino[1], I. Morales[3], E. Mujica[5], G. Páez[7], E. Sánchez-Blanco[5], S. Tulloch[5], M. Velázquez[2], J. Zamorano[1], A. Aguerri[8], D. Barrado[9], E. Bertone[2], C. Catalán-Torrecilla[1], A. Cava[10], S. Cazzoli[3], J. Cenarro[11], M. Chamorro-Cazorla[1], M. Chávez[2], M. García[9], J. García-Rojas[8], R. González Delgado[3], J. Guichard[2], R. Guzmán[12], B.T. Dullo[1], A. Herrero[8], N. Huélamo[9], D. Hughes[2], J. Jiménez[13], C. Kehrig[3], I. Márquez[3], J. Masegosa[3], D. Mayya[2], J. Méndez Abreu[8], M. Mollá[14], C. Muñoz Tuñón[8], N. Noughani[15], A. del Olmo-García[1], M. Peimbert[16], P. Pérez González[1], E. Pérez Montero[3], S. Roca-Fàbrega[1], M. Rodríguez[2], J.M. Rodríguez Espinosa[8], L. Rodríguez[2], D. Rosa[2], J. Sánchez Almeida[8], C. Sánchez Contreras[9], P. Sánchez Blázquez[1], S.F. Sánchez[16], A. Sarajedini[12], S. Silich[2], S. Simón-Díaz[8], G. Tenorio Tagle[2], E. Terlevich[2], R. Terlevich[2], S. Torres-Peimbert[16], I. Trujillo[8], Y. Tsamis[17], O. Vega[2] and V. Villar[1]

*(Affiliations can be found after the references)*

Received September 15, 1996; accepted March 16, 1997

**ABSTRACT**

*Context.* Since its commissioning at the Gran Telescopio Canarias (GTC) on August 2017 the MEGARA intermediate-resolution fiber-based optical spectrograph provides GTC with an unprecedented combination of versatility and performance for a 10 m-class telescope offering both Integral Field and Multi-Object Spectroscopy capabilities, spectral resolutions in the range R=6 000-20 000 thanks to the use of a total of 18 high-efficiency VPHs, and a wide spectral coverage from 365-970 nm.

*Aims.* As a GTC facility instrument, MEGARA was designed with the aim of covering broad range of scientific objectives, from the mapping of nebular objects, both Galactic and extragalactic, in Integral-Field spectroscopy to the analysis of individual stars in Milky Way and the Local Group and distant galaxies. In a record time of three years after its detailed design was finalized, MEGARA was sent to GTC in March 2017 receiving first light on June 24$^{th}$ 2017. MEGARA was offered to the GTC community starting on July 2018, as part of 2018B observing period.

*Methods.* In this paper we present the results of the MEGARA integration and commissioning phases, when the instrument high-level scientific requirements were validated. In addition to the nominal tests carried out to determine the focal-plane spaxel-to-spaxel uniformity, MOS robotic positioners' performance and spectral resolution, wavelength coverage and efficiency associated to its 18 VPH-based spectral setups (6 LRs, 10 MRs and 2HRs) we also present the results on its scientific validation on sky using as examples the IFU observations of BD+33 2642 and the MOS spectroscopy of Globular Cluster M 15

*Results.* .

*Conclusions.* The performance of both the MEGARA Integral-Field and Multi-Object modes in all their 18 spectral setups were successfully tested. The scientific validation demonstrated that the unique combination of versatility, efficiency and spectral resolution of MEGARA in combination with the unsurpassed collecting area of the telescope have opened several niches for the scientific exploitation of GTC.

**Key words.** Astronomical instrumentation, methods and techniques – Instrumentation: spectrographs – Techniques: imaging spectroscopy – Techniques: spectroscopic

## 1. Introduction

The design of astronomical instruments necessarily involves a number of trade-offs among the different parameters that define it. Optical spectrographs are not different, with compromises typically being made between spectral resolution, multiplexing, efficiency, and wavelength coverage. Most optical spectrographs to date have prioritized either efficiency or spectral resolution. High efficiencies commonly imply low-multiplexing or low spectral resolution designs, such as those of single-fiber/long-slit or (most) grism-based/integral-field spectrographs, respectively. Moreover, in an attempt to provide either very high spectral resolution or a fair combination of multiplexing, efficiency and (moderate) spectral resolution versatility is often lost. Thus, some of the most successful instruments to date, such as HARPS (Mayor et al. 2003), SAURON@WHT (Bacon et al. 2001) or MUSE@VLT (Bacon et al. 2010), provide virtually a single, fixed observing mode and spectral configuration.

MEGARA, which stands for *Multi-Espectrógrafo de Alta Resolución para Astronomía* (in Spanish), has been designed with the aim of providing the Gran Telescopio Canarias (GTC hereafter) with both Integral-Field (IFU hereafter) and Multi-Object (MOS hereafter) capabilities with the highest multiplexing possible at spectral resolutions R=6 000 and R=12 000 in the entire optical range (reaching up to R=20 000 in specific spectral windows) while maximizing efficiency and, to a lesser extent, spectral coverage. As a common-user facility instrument, this unique combination of versatility, spectral resolution and efficiency (especially when combined with the large collecting area of GTC) should serve the GTC community to break

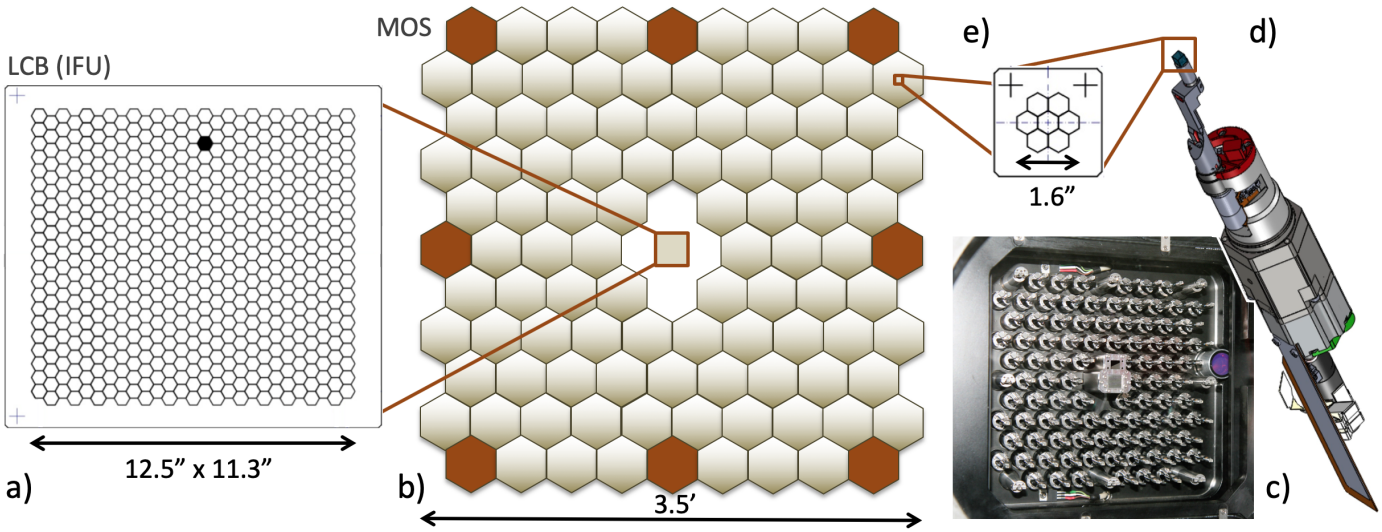


**Fig. 1.** Focal-plane layout of the MEGARA instrument. **a)** Layout of the 567 optical fibers of the MEGARA LCB mode. In black we identify the single broken fiber of the IFU. The position of the reference marks used during the alignment process are also shown. **b)** Light-colored hexagons represent the position and non-overlapping parts of the patrol area of each of the 92 positioners of the MEGARA Fiber-MOS. The actual patrol areas are overlapping circular regions of 28 arcsec in diameter within which one can place each of the 92 microlens arrays shown in panel e). The hexagons colored in orange represent the position of the eight fixed 7-fiber minibundles used for sky subtraction for the LCB. **c)** Photograph of the Fiber-MOS seen from the telescope side. The LCB mechanical frame, the top part of the 92 robotic positioners and the boresight telescope (at right in the image, for alignment of the instrument reference mechanical frame with the exit pupil of GTC) are clearly seen. **d)** Final design of the MOS robotic positioners. **e)** Microlens array attached to each of the 92 MOS robotic positioners and 8 sky minibundles.

new ground in multiple research fields, from the detailed analysis of nearby stars and stellar clusters to the study of the first (narrow-lined) galaxies. Similar combinations of IFU plus MOS capabilites, efficiency and spectral resolution are being targeted by remarkable ongoing instrumental efforts, such as WEAVE@WHT (Dalton et al. 2018) or MOSAIC@ELT (Hammer et al. 2016). Worth mentioning precursors of MEGARA in this regard are the FLAMES fiber link (Pasquini et al. 2002) combined with the GIRAFFE spectrograph (Hammer et al. 1999) at VLT and the AAOmega spectrograph at the AAT (see Sharp et al. 2006). However, none of the two reach the light grasp of MEGARA@GTC albeit their similar spectral resolutions.

GTC is a 10.4 m telescope located at the Roque de los Muchachos observatory in La Palma (Spain) at an elevation of 2300 m. It is owned by a Consortium composed by Spain, two Mexican research centers (INAOE & UNAM) and the University of Florida (USA). In addition to MEGARA, GTC counts with three other facility instruments: the optical imager and low-resolution spectrograph OSIRIS (Cepa et al. 2003), the mid-infrared imager CanariCam (Telesco et al. 2013) and the near-infrared imager and low-to-intermediate resolution spectrograph EMIR (Garzón et al. 2016). MEGARA joined the GTC instrument suite on August 31$^{st}$ 2017 when the instrument commissioning was successfully completed in both its modes and in all 18 spectral configurations available for each mode. In this paper we introduce the main characteristics of the instrument (Section 2), the results of the commissioning tests performed to verify the instrument performance (Section 3) and a description of the on-sky observations carried out during its night-time commissioning (Section 4). Finally, our conclusions are summarized in Section 5.

## 2. MEGARA Characteristics

The MEGARA instrument is composed of two different units separated by a fiber link of 44.5 m in length, namely the *Fiber-MOS*, which is placed in the Folded-Cassegrain focus F (FC-F hereafter) of GTC, and the *MEGARA spectrograph*, which is located in its Nasmyth A platform. A summary of the main parameters of the instrument is given in Table 1. In this section, we describe the main characteristics of these two units along with the fiber link itself.

**Table 1.** Main parameters of the MEGARA instrument.

| Parameter | Value |
|---|---|
| IFU (LCB) FoV | $12.5 \times 11.3$ arcsec$^2$ |
| MOS FoV | $3.5 \times 3.5$ arcmin$^2$ |
| Spaxel size (LCB/MOS) | 0.62 arcsec (diameter of circle inscribing the hexagon) |
| Wavelength range | 365–970 nm |
| Spectral resolution[a] | 6 000 (LRs) |
| | 12 000 (MRs) |
| | 20 000 (HRs) |
| Multiplexing LCB | 567 IFU + 56 sky fibers |
| Multiplexing MOS | 7 fiber x 92 bundles |
| GTC foci | Folded-Cass. F (Fiber-MOS) |
| | Nasmyth A (spectrograph) |

[(a)] These are measured values, which exceed the requirements at high spectral resolutions (see text and also Table 2).

### 2.1. Fiber MOS

Although this unit is responsible from collecting the light at the FC-F focus of GTC for both MEGARA modes, IFU and MOS, its name reflects the larger complexity of the MOS component in terms both of hardware and software compared to the IFU. In Figure 1 we show the layout of MEGARA in the FC-F focal plane of the telescope. While the IFU (also called Large Compact Bundle; LCB hereafter) collects the light in the central 12.5×11.3 arcsec$^2$ of the focal plane, where aberrations are

minimal, the MOS fills the flat and unvignetted FC-F focal plane of GTC covering an area of 3.5×3.5 arcmin$^2$, except for the central gap left for the LCB. At the plate scale of GTC, 1.212 arcsec mm$^{-1}$ (or F/∼17, common to all its foci), the physical dimensions become ∼1 cm$^2$ and 17×17 cm$^2$, respectively for the LCB IFU and the MOS. This intermediate focal ratio along with the scientific requirements of the MEGARA science team and the multiplexing limits imposed at the level of MEGARA's single spectrograph drive the characteristics and MEGARA and, to some extent, also its uniqueness.

The first element of this unit is a fused-silica field lens that corrects for the non-telecentricity of GTC, so all MOS robotic positioners, independently of the distance to the optical axis are mounted in a common, flat mechanical frame is also confocal with the LCB. This lens introduces basically no power neither changes the plate scale at the instrument focal plane. In order to minimize losses due to Focal-Ratio Degradation (FRD hereafter) at the exit of the fiber link, the input F/17 beam is then converted to F/3 by microlenses made of fused silica. Each microlens has a hexagonal shape and it is inscribed in a circle that projects 0.62 arcsec on the sky in diameter (see more details in Pérez-Calpena et al. 2012, 2014). Identical microlenses are used for both the LCB and the MOS modes. In the case of the LCB a total of 567 microlenses are distributed in a rectangular hexagonally-packed area (see Figure 1). The hexagonal packing is optimal for minimizing losses in between spaxels while the rectangular shape allows for an efficient mapping with low redundancy. In addition to the fibers in this compact bundle, the IFU mode also includes a total of 56 (also identical) sky fibers that are arranged in 8 fixed minibundles of 7 fibers each that are located at the four corners and the four lateral sides of the instrument FoV, at distances ranging between 1.75-2.5 arcmin. The procedure used to allow for a precise alignment between the telescope pupil image formed by each of the microlenses and the corresponding fiber core is described in detail in Pérez-Calpena et al. (2016).

Regarding the MOS mode, a total of 92 robotic positioners, each holding a microlens array composed of 7 hexagonal spaxels that cover altogether 1.6 arcsec in diameter on the sky (see Figure 1), span an area of 3.5×3.5 arcmin$^2$ by means of 92 overlapping circular patrol areas of 28 arcsec in diameter. Each of these circular patrol areas are covered by means of the interpolation of two closed-loop rotations, one going from 0 to 365° around the positioner geometrical axis and another one that can rotate from 0 to 185° around an axis offset by 7 arcsec from the center of the positioner. The assignment of targets and the optimal sequence of motion for the positioners are computed using dedicated control software (Castillo-Morales et al. 2013).

The MEGARA Fiber-MOS unit also incorporates a focal-plane cover which allows to block each half of the field separately while letting the other half being illuminated and registered by the instrument (in the vertical direction as shown in Figure 1). Given the spatial arrangement of the optical fibers in the field and on the pseudo-slits, by covering one side of the field the user can block the light coming to one of every two fibers on the MEGARA detector for the LCB and one of every two positioners for the MOS. This drastically reduce the level of crosstalk in between adjacent fibers/positioners on the pseudo-slits by cutting the available FoV by a more than half. In this latter regard, we note that although the cover is placed very close to the focal surface of the microlenses, the central ∼2 arcsec-wide vertical strip of the LCB and the positioners placed along this same vertical divider always receive light from the telescope given the finite size of the incoming beam at the position of the cover.

The 623 fibers from the LCB mode (including the 56 sky fibers) and the 92×7 fibers from the MOS leave the FC-F focus station through the corresponding rotator (which has also the capability of changing the Fiber-MOS Position Angle on the sky) and, after driving the light along the telescope ring and through the elevation rotator, arrive to the Nasmyth A platform where the MEGARA spectrograph is located. All the 1267 Polymicro-FBP 100/140/170 (core/cladding/coating) optical fibers are identical and have a length of 44.5 m each and a numerical aperture of 0.20±0.02. They travel in coated 7-fiber minibundles that are packed in two separate bundles, LCB and MOS. In the next section we detail the arrangement of the fibers on the corresponding LCB and MOS pseudo-slits as part of the description of the MEGARA spectrograph (see more details in Pérez-Calpena et al. 2014).

### 2.2. Spectrograph

The MEGARA spectrograph is a fully-reflective collimator-camera system composed of 12 lenses, five part of the F/3 collimator (including an aspheric singlet and two doublets) and seven in the F/1.5 camera (three singlets and two doublets), both elements placed in a 68° fixed-angle configuration. The 160 mm free-aperture pupil is located in between these two elements, where the disperser forms an angle of 34° with each of them (see Carrasco et al. 2016).

The entrance focal plane of the spectrograph is curved and telecentric. The technical solution to account for such curvature and telecentricity was to arrange the LCB (MOS) fibers in a 111 mm (118 mm)-long pseudo-slit composed of a total of 17 (19) flat boxes that altogether reproduce the focal-plane 1075 mm-long radius of curvature. Inside each box the fibers were put side by side and polished at once. The distance between adjacent fiber cores in the pseudo-slits was set by the fiber coating (170 $\mu$m) except for the first and last fiber of each box where the distance is roughly twice that value due to the need of the use of mechanical references in between boxes. As shown in Section 3, this design yields an EED$_{80}$ better than 60 $\mu$m (or four detector pixels) at the camera focal plane for our 100 $\mu$m-core fibers.

After the first lens of the collimator (a PBM2Y-glass high-order aspherical), a rotating shutter allows to select among three different configurations: *closed*, *open-blue* (equipped with a short-pass filter with $\lambda_{\rm cutoff}$=6700 Å) and *open-red* (order-sorter filter with $\lambda_{\rm cutoff}$=5700 Å), so all spectral setups are approximately confocal, albeit slightly wavelength dependent. The change of focus for each spectral setup, which requires a motion along the optical axis, and of pseudo-slit in between LCB and MOS, which needs of a fixed displacement perpendicular to the optical axis for the corresponding slit to face the entrance of the collimator, are achieved by means of a x-y mechanism on which both pseudo-slits are mounted.

As part of the design optimization of the MEGARA spectrograph a total of 18 different spectral setups were validated. All setups and all fibers and wavelengths within each setup were given equal weight when determining the most optimal design parameters. These 18 spectral setups correspond to the same number of Volume Phase Holographic gratings (VPH hereafter). Out of these 18 VPHs, six yield $R\sim6\,000$ (low-resolution; LR hereafter), ten yield $R\sim12\,000$ (medium-resolution; MR hereafter) and two reach $R\sim20\,000$ (high-resolution; HR hereafter), where $R$=$R_{\rm FWHM}$=$\lambda/\Delta\lambda_{\rm FWHM}$. These resolving powers are the actual on-sky values at the central wavelength of each VPH,

which, especially for the MRs and HRs, are slightly better than the requirement (see Table 2). The angular dispersion of these VPHs along with the wide range output angles reaching the camera (±7°) and its focal length (246 mm) yield a variation of ∼ ±20% in $R$ within each spectral setup on the detector (see Figure 2).

The hologram of the LR VPHs is a gelatin that is sandwiched between two flat windows, so the incident angle of the light on the hologram is only modified by the window refraction index. However, for MR and HR VPHs was necessary to also include prisms at each side of the flat windows to yield the required resolving powers using holograms with less than 5,000 lin mm$^{-1}$. The apex angles for these prisms are 44° in the case of the MRs and ∼68° for the HRs. Thus, given the required optical apertures (up to 180×220 mm$^2$), large sizes (e.g. 250×250×200 mm$^3$ for MRs) and glass densities (∼3.6 gr cm$^3$), the resulting weights for each MR and HR setup is ∼30 kg, mount included.

As it can be seen in Figure 2, the LR and MR VPHs cover the entire optical window from 365 nm to 970 nm at their respective resolutions, while the HR-R VPH covers the [N II]$\lambda\lambda$6548,6584ÅÅ+H$\alpha$ and [S II]$\lambda\lambda$6717,6731ÅÅ sets of lines at redshifts z<0.032 and z<0.01, respectively, and the HR-I VPH covers the so-called near-infrared Calcium Triplet region. More information about the design, manufacturing, integration and subsystem tests of the MEGARA VPHs can be also found in Izazaga et al. (2016) and Martínez-Delgado et al. (2016).

In order to place a specific VPH in the pupil, MEGARA counts with an insertion mechanism that extract the VPH from a rotating wheel and put it in the pupil with sub-pixel repeatability. The VPH wheel can host up to 11 VPHs simultaneously and, combined with the insertion mechanism, allows changing the instrument spectral configuration in less than one minute.

As mentioned above, the camera collects the light coming out from the VPHs in angles between ±7°, which, once projected on the MEGARA detector, leads to the spectral ranges covered by each VPH shown in Figure 2. Note that the mild C distortion of the spectrograph yields slightly different wavelength ranges for each fiber. In Table 2 we provide the spectral ranges available to each VPH as those minimum and maximum wavelengths covered either by at least one fiber ($\lambda_{\rm min,1}$,$\lambda_{\rm max,1}$) or common to all fibers ($\lambda_{\rm min,all}$,$\lambda_{\rm max,all}$).

The MEGARA detector is a E2V (now Teledyne) deep-depleted Charge-Coupled Device (CCD) model 231-84 using the Astro Multi-2 AR coating. It contains a total of 4096×4112 pixels of 15 $\mu$m in size and can be read through a maximum of four outputs. The MEGARA CCD is read using only two diametrically opposed amplifiers to achieve a 40 s readout at <3 e$^-$ noise whilst minimizing cross talk within the device (see e.g. Reiss et al. 2012). The CCD is mounted in a closed-cycle LN2 cryostat designed and built at INAOE (see Ferrusca et al. 2014) that is kept horizontally on the spectrograph optical bench and where the last camera lens also acts as vacuum window. The cryostat has two main componentes, the CCD head and the dewar back. In the CCD head, a thermal isolating mounting supports the CCD 6-degree kinematic mounting and the CCD PCB. The CCD is thermally connected to the LN2 tank through a high-purity oxygen-free copper strap maintaining an operating temperature of 158 K for a hold-time of ≥40 h. The CCD is connected to the PCB by flex cables that send the signals out through hermetic connectors on the vacuum shroud. The aluminum dewar back serves as vacuum jacket and contains the 7.3 liters-tank of LN2. For a more detailed description of the MEGARA CCD and Cryostat see Castillo-Domínguez et al. (2012). More info on the detailed CCD characterization performed at the LICA-UCM laboratory can be found in Tulloch et al. (2012, 2013; see also Zamorano et al. 2013).

The optical design and as-built laboratory performance of the MEGARA spectrograph are extensively discussed in Carrasco et al. (2016), while the delivery of the instrument to the GTC site is presented in Pérez-Calpena et al. (2018a). In Section 3 we provide the results regarding the instrument performance obtained on-site while in Section 4 we demonstrate the unique capabilities of MEGARA by showing some examples of astronomical targets observed in different VPHs and modes (LCB and MOS) during the night-time commissioning phase.

### 2.3. Data Reduction

For a fiber-based instrument with high multiplexing and multiple modes the use of a custom-made set of processing recipes is a must. In our case this work is done by the python-based MEGARA Data Reduction Pipeline or `megaradrp` (Pascual et al. 2018, 2019).

The processing steps carried out by `megaradrp` include the bias subtraction, trimming, tracing and extraction, wavelength calibration, fiber-flat fielding, and flux calibration (see Castillo-Morales et al. 2018). Each of these tasks corresponds to a different reduction recipe. The final products generated by each recipe include a master bias image (bias subtraction), trace map (tracing), wavelength and $\Delta\lambda_{\rm FWHM,\lambda_c}$ maps (see Figure 3) for all illuminated pixels in the detector (wavelength calibration), pixel-to-pixel relative sensitivity map (fiber-flat fielding) and a system sensitivity function. The processing of LCB (MOS) images yields a flux-calibrated multi-extension Row-Stacked-Spectra (RSS hereafter) FITS frame that includes 623 (644) 4300-element flux vectors and positions on the sky of every single fiber and, in the case of the MOS, also of every 7-fiber collapsed mininbundle. The RSS frames of the same VPH all share the same common initial lambda and reciprocal dispersion (see Table 2). As part of the procedure for extracting the flux in each fiber, in addition to the use of fixed aperture around each trace, `megardrp` also provides the results from a simultaneous fit to all 623 (644) fiber profiles (peak fluxes, positions and sigmas as a function of wavelength) using LCB (MOS) halogen-lamp observations. This allows correcting for cross-talk in between the spectra of adjacent fibers in the detector, that is estimated to be in any case below 5-7% in the central pixel found in between two equally-illuminated fibers. The processing of the LCB and MOS images yields RSS images with and without the sky being subtracted. By default, the sky spectrum is obtained from the 56 sky fibers in the case of the LCB or from all fibers identified as BLANK in the MOS configuration file delivered to GTC as part of the Phase 2 proposal submission.

In order to modify the parameters used during the data reduction the `megaradrp` uses YAML configuration files. Given that the spectrograph is kept static in the Nasmyth A platform of GTC, the positioning of the pupil elements is highly repeatable and the spectrograph image quality is not altered by the observing conditions, these parameters are highly uniform with time. In that regard, we note that the focus of the spectrograph is automatically adapted to the instrument temperature estimated by a series of sensors distributed over the optical bench. As discussed in Section 3, the only parameter that requires special attention is a global offset in the spatial position of all fibers when the temperature present when the halogen-lamp observations used for fiber tracing were taken and that of the scientific target acquisition differ in more than one degree.

**Table 2.** Properties of the 18 spectral configurations of MEGARA in the LCB mode.

| Setup | VPH name | $\lambda_{min,1}$ (Å) | $\lambda_{min,all}$ (Å) | $\lambda_c$ (Å) | $\lambda_{max,all}$ (Å) | $\lambda_{max,1}$ (Å) | $R$ (=$R_{FWHM}$) ($\lambda/\Delta\lambda_{FWHM,\lambda_c}$) | $\Delta\lambda_{FWHM,\lambda_c}$ (Å) | $\delta\lambda$ (Å pixel$^{-1}$) |
|---|---|---|---|---|---|---|---|---|---|
| (1) | (2) | (3) | (4) | (5) | (6) | (7) | (8) | (9) | (10) |
| LR-U | VPH405-LR | 3640.04 | 3654.32 | 4025.90 | 4391.88 | 4417.33 | 6028 | 0.672 | 0.195 |
| LR-B | VPH480-LR | 4278.43 | 4332.05 | 4785.32 | 5199.96 | 5232.02 | 6059 | 0.792 | 0.230 |
| LR-V | VPH570-LR | 5101.13 | 5143.74 | 5678.63 | 6168.19 | 6206.04 | 6080 | 0.937 | 0.271 |
| LR-R | VPH675-LR | 6047.62 | 6096.54 | 6729.61 | 7303.21 | 7379.88 | 6099 | 1.106 | 0.321 |
| LR-I | VPH799-LR | 7166.47 | 7224.11 | 7976.31 | 8640.37 | 8822.29 | 6110 | 1.308 | 0.380 |
| LR-Z | VPH890-LR | 7978.45 | 8042.74 | 8873.16 | 9634.92 | 9692.58 | 6117 | 1.455 | 0.421 |
| MR-U | VPH410-MR | 3911.99 | 3919.81 | 4102.87 | 4282.17 | 4289.11 | 12602 | 0.326 | 0.092 |
| MR-UB | VPH443-MR | 4217.44 | 4226.38 | 4429.44 | 4625.79 | 4633.65 | 12370 | 0.358 | 0.103 |
| MR-B | VPH481-MR | 4575.84 | 4585.66 | 4809.46 | 5025.07 | 5033.66 | 12178 | 0.395 | 0.112 |
| MR-G | VPH521-MR | 4952.15 | 4963.22 | 5208.79 | 5445.00 | 5454.62 | 12035 | 0.433 | 0.126 |
| MR-V | VPH567-MR | 5369.03 | 5413.11 | 5664.96 | 5923.90 | 5659.56 | 11916 | 0.476 | 0.135 |
| MR-VR | VPH617-MR | 5850.19 | 5894.23 | 6165.79 | 6448.52 | 6468.52 | 11825 | 0.522 | 0.148 |
| MR-R | VPH656-MR | 6228.15 | 6243.10 | 6560.33 | 6865.26 | 6878.27 | 11768 | 0.558 | 0.163 |
| MR-RI | VPH712-MR | 6748.88 | 6764.58 | 7109.81 | 7440.85 | 7454.46 | 11707 | 0.608 | 0.172 |
| MR-I | VPH777-MR | 7369.39 | 7386.53 | 7765.14 | 8127.95 | 8142.75 | 11654 | 0.666 | 0.189 |
| MR-Z | VPH926-MR | 8787.88 | 8810.52 | 9274.84 | 9698.97 | 9740.20 | 11638 | 0.796 | 0.222 |
| HR-R | VPH665-HR | 6397.62 | 6405.61 | 6602.59 | 6797.14 | 6804.87 | 18700 | 0.355 | 0.098 |
| HR-I | VPH863-HR | 8358.64 | 8380.20 | 8626.01 | 8882.38 | 8984.87 | 18701 | 0.462 | 0.130 |

**Notes.** Column 1: Spectral setup (VPH short name). Column 2: VPH full name. Column 3: Shortest wavelength reached by at least one fiber. Column 4: Shortest wavelength common to all fibers. Column 5: Central wavelength for central fiber. Column 6: Longest wavelength common to all fibers. Column 7: Longest wavelength reached by at least one fiber. Column 8: Resolving power requirement at the central wavelength. Column 9: Spectral resolution requirement at the central wavelength. Column 10: Average linear reciprocal dispersion (constant wavelength dispersion solution adopted during the reduction process by the MEGARA Data Reduction Pipeline). Columns 3-6 are on-sky measurements while columns 8 and 9 represent design requirement values. As shown in Figure 2, measured values improve these numbers in the majority of fibers in the pseudo-slit, especially in the case of MR and HR VPHs. Values quoted for every setup are virtually identical in the case of the MOS mode.

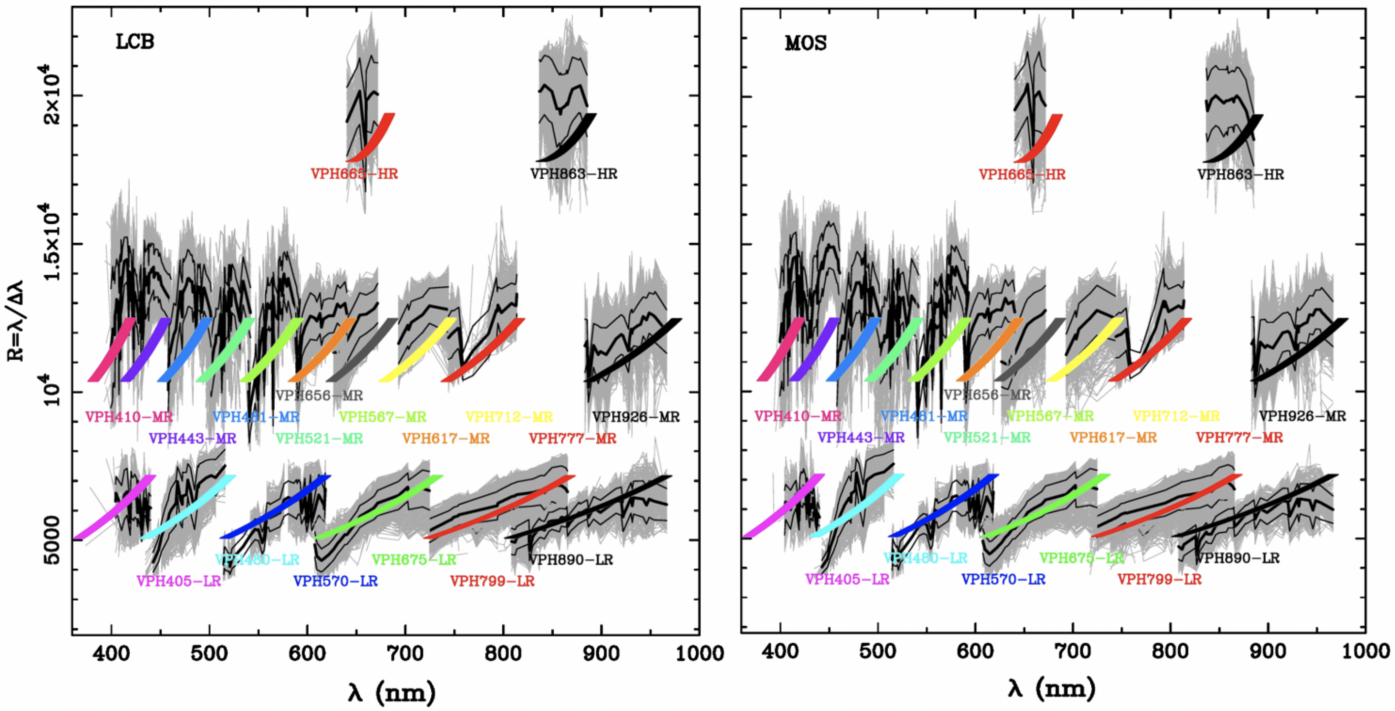


**Fig. 2.** Relation between resolving power ($R_{FWHM}$) and wavelength coverage for all 18 MEGARA VPHs and for the LCB (left) and MOS (right) modes. Both design values (colored lines) and laboratory-integration measurements (grey and black lines) are shown. The grey lines connect the measurements obtained from individual ThAr/ThNe arc lines across each VPH wavelength range for individual fibers, while black thick and thin lines represent the mean and mean ± 1 $\sigma$ curves when all fiber spectra are considered, respectively. Note that while the average curves nicely match the requirements in the case of the LR VPHs, they exceed the requirement in most fibers in the case of the MR and HR VPHs. This is due to the fact that image quality in the LR setups is limited by need of simultaneously focusing a wider range of wavelengths. The lack of data below ~4000 Å is due to the fact that the halogen lamps at the FC-F ICM provided by GTC do not yield enough signal for tracing below that wavelength.

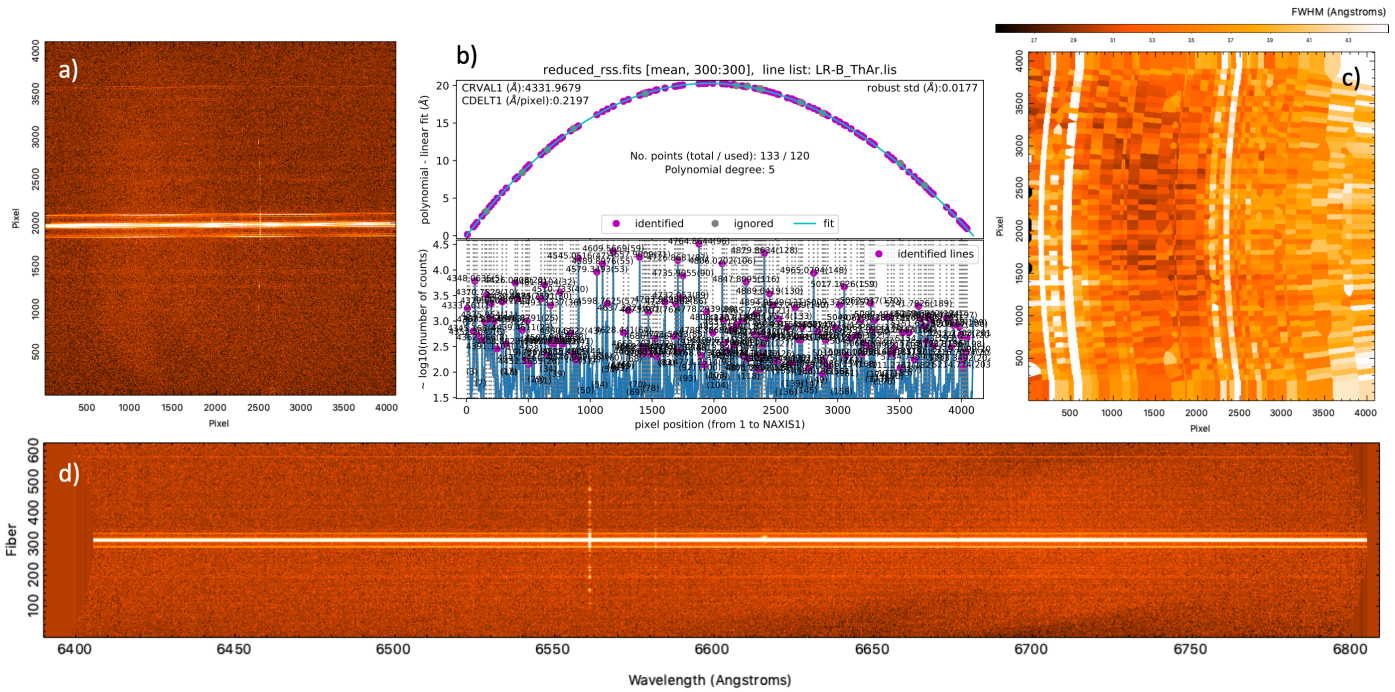


**Fig. 3.** Examples of data products generated by `megaradrp`. **a)** Pre-processed raw image in the HR-R setup of first-light target BD+33 2642 observed in this case for 3×120 seconds on the night of June 26$^{th}$ 2019. The level of preprocessing here only includes the removal of the prescan and overscan regions of the two amplifiers, the subtraction of the bias image and the combination of three individual images. **b)** Results of the wavelength calibration solution for a specific fiber (#306) in the spectral setup LR-B for a ThAr arc observation. Note that all fibers for each setup in the resulting RSS are processed to a common linear dispersion solution, in this case with a initial wavelength of 5870 Å and a (constant) reciprocal dispersion of 0.1445 Å pixel$^{-1}$. **c)** This image represents the Voronoi map generated by `megaradrp` from all measurements of the FWHM of 622×40 individual spectral lines times fibers identified in a combination of three ThAr arc images in the LR-B setup. White columns correspond to partially resolved ThAr multiplets that lead to large apparent FWHM values. **d)** Final RSS image obtained from the pre-processed HR-R image shown in panel a). Note that while in the image shown in panel a) the wavelength increases from right to left, in the final RSS image it is the opposite. This latter image shows the very extended line emission of this post-AGB/pre-PN object that goes beyond that previously reported by Napiwotzki et al. (1994) (see Section 4).

The `megaradrp` is optimized for python 3.x but it is also compatible with python 2.x and can be installed as an `anaconda` package or via `virtualenv`. The processing of MEGARA (or EMIR) data requires also of the installation of the `numina` GTC processing environment. Both `numina` and `megaradrp` are available through `github`[1], the GTC website and the `Zenodo` repository (Pascual et al. 2018). In the latter case, we also provide calibration files (arc-line catalogs, master traces and wavelength solutions) for all 18×2 setups in Cardiel & Pascual (2018).

More info on the MEGARA Data Reduction Pipeline can be found in Pascual et al. (2019, in prep.).

## 3. Instrument performance

The MEGARA instrument arrived to the GTC facilities on March 28$^{th}$ 2017. After 14 days split in three periods on April 2017 devoted to the integration of the two units plus the fiber routing, the daytime commissioning started on May 8$^{th}$. This phase lasted until June 9$^{th}$. On June 24$^{th}$ 2017 the instrument had its on-sky first light on the spectrophometric standard star BD+33 2642 and surrounding pre-Planetary Nebula PN G052.7+50.7 (see Figure 3 and Section 4). That night also marked the beginning of the nighttime commissioning, which ended on August 31$^{st}$ 2017. The first Open-Time observations took place on July 2018, as part of the 2018B regular GTC observing semester.

[1] `https://github.com/guaix-ucm/megaradrp`

In this Section we describe the results of the main commissioning tests (both daytime and nighttime ones) designed to verify the performance of the instrument and the fulfillment of its design requirements (see Table 1).

Right before the onset of the commissioning phase, we evaluated the alignment of the instrument optical axis with both the telescope optical axis at the FC-F focal station and its corresponding rotator. In order to do that the instrument has a boresight telescope (see Figure 1) that is aligned with the instrument optical axis and that is designed to take images of the telescope pupil using a commercial CCD camera, which in the case of GTC is located at the secondary mirror. The results of the analysis of these images using different rotator angles were that the alignment of the MEGARA Fiber-MOS assembly with the FC-F rotator axis was below 0.5 arcmin but that a misalignment with respect of the FC-F optical axis of ∼5 arcmin was present. This misalignment was confirmed by GTC as due to the telescope tertiary mirror and corrected after the end of the commissioning phase of MEGARA.

### 3.1. Folded-Cassegrain unit performance

Although the optical-axis misalignment problem might result in an average loss of ∼2 % of the light that should reach the optical fibers from each pupil image, we could still validate the optical alignment and spaxel-to-spaxel uniformity of both the LCB and MOS modes separately using measurements of the flux received

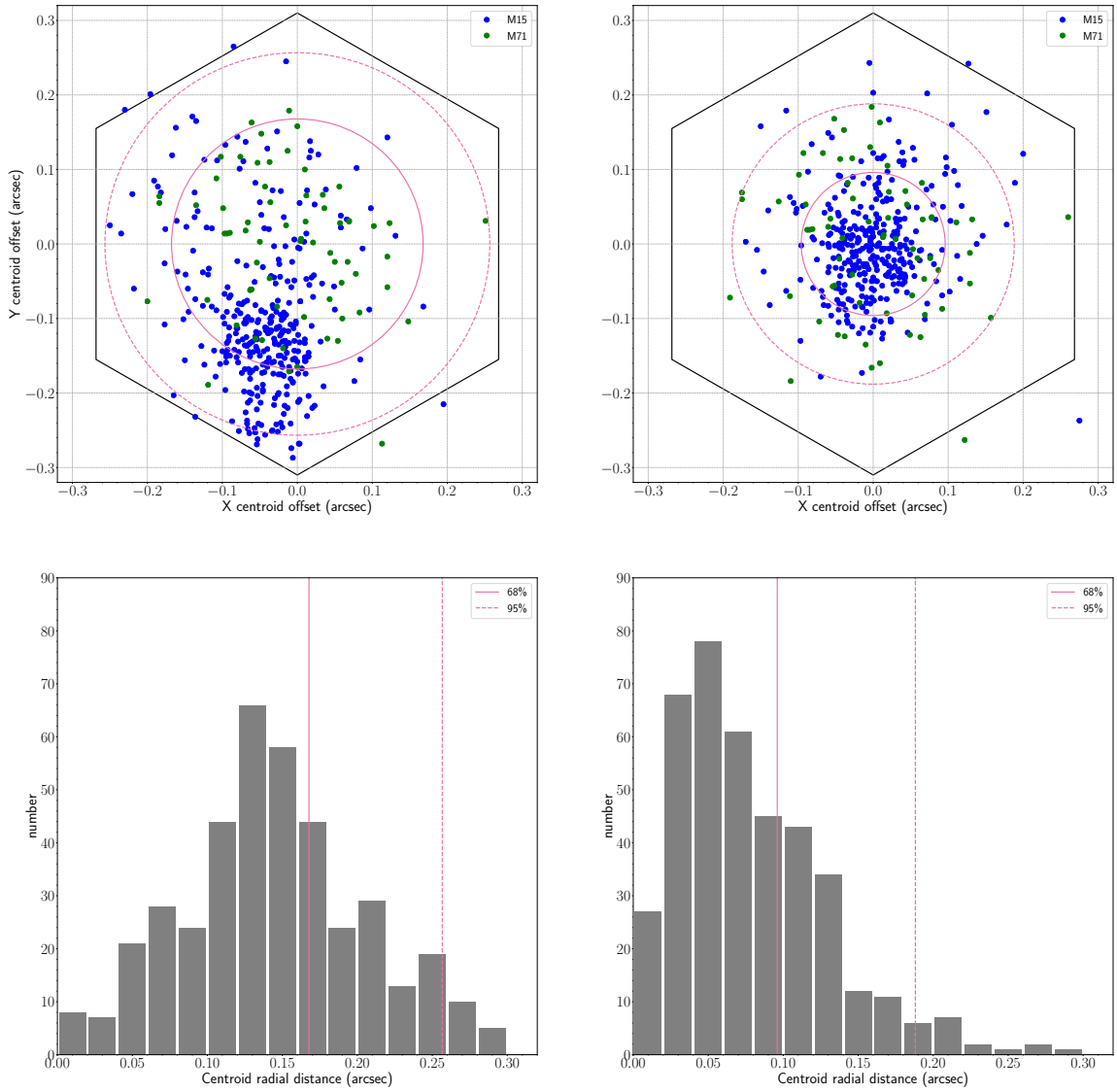


**Fig. 4.** Top plots: Distribution of the centroids computed for all 333 M15 stars (four pointings with multiple stars in common among all pointings) and 67 M71 stars (one pointing) assigned to robotic positioners of the MEGARA MOS. The nominal (optimal) position should be zero as this would coincide with the center of each seven-spaxel minibundle. The size of the central hexagonal spaxel is outlined. Bottom plots: Frequency histogram of radial distances with the 67% and 95% best centroids shown as vertical solid and dashed lines, respectively. These lines correspond to the dashed circles shown in the top plots. Left panels: Centroids obtained from the level of continuum flux (averaged over the entire LR-R VPH spectral range) without any global correction). Right panels: Centroids derived after each pointing has been corrected for a global offset introduced during the acquisition. A more careful acquisition, e.g. by using guide stars that would not require to move the guide probe in between the LCB acquisition and the MOS observation, should be able to reduce these global offsets to no more than ∼0.1 arcsec.

on the detector for all fibers in images all ICM halogen-lamp, dome flat and twilight-sky images for different instrument rotator angles. Even for a perfect optical axis alignment and in spite the fact that in MEGARA the images of the pupils are slightly oversized on the fiber cores to maximize flux homogeneity, a static spaxel-to-spaxel variation in sensitivity is expected due to potential misalignments between pupil images and fiber cores (e.g. for those cases close to our 10 $\mu$m alignment precision requirement), the non-circular shape of the GTC pupil image, variations in sensitivity throughout the microlens array and the fiber-to-fiber sensitivity and focal-ratio-degradation (FRD) variations. Thus, for a fixed FC-F rotator angle the observation of dome flat and twilight-sky images in a total of 5 different VPHs (namely LR-I, LR-R, LR-Z, MR-B and MR-G) yielded spaxel-to-spaxel variations of less than 8 % in all cases and for both LCB and MOS. The (also static) component of inhomogeneity due to changes in the non-circular pupil projection with the FC-F rotator angle (relative to the fixed-angle observations above) yielded variations below 5 % for the LCB and 10% MOS. The larger value obtained for the MOS could be due to an additional global optical axis misalignment of the MOS mechanical frame or, more likely, to the tilt of the buttons defining the optical axes of each of the 92 individual positioners relative to the MOS mechanical frame.

In the case of the MOS we should also consider flux variations due to the changes in tilt associated to different (dynamic) configurations of the robotic positions. This dynamical component was found to be also lower than 10 % for all robotic posi-

tioners but #33 (12 %). It should be noted that these two latter components (LCB & MOS static one for different rotator angles and the MOS dynamical one) include the ∼2 % variation due to the aforementioned problem of misalignment of the telescope optical axis present at the time of the instrument commissioning. We highlight here that the fulfilment of our 10 % MOS homogeneity requirement relied on a detailed static and dynamical tilt budget for each and all the 92 MOS robotic positioners (see Pérez-Calpena et al. 2018b).

As part of our nighttime commissioning observations we obtained LR-R MOS spectra of a number of 333 and 67 red luminous stars (mainly Red-Giant stars; see García-Vargas et al. 2020) in the Galactic Globular Clusters (GCs) M15 and M71, respectively. M15 stars were observed in four different MOS pointings on July 31$^{st}$ 2017 and August 29-30$^{th}$ 2017 while the M71 stars were observed in one single pointing acquired on July 31$^{st}$ 2017. The proximity of these GCs allowed us to place bright stars (G<16 mag) in the majority of the MEGARA robotic positioners. In Figure 4 we show the centroids computed using the LR-R continuum flux from the seven fibers within each MOS minibundle for all stars that could have a robotic positioner assigned. In order to acquire the field we first used the LCB to place a bright reference star near the nucleus of the corresponding GC in the center of the LCB. We then changed from LCB to MOS mode (in just a few seconds by moving the pseudo-slit mechanism) and started guiding and integrating on the GC stars that cover the entire 3.5×3.5 arcmin$^2$ MOS FoV.

The left panel of Figure 4 shows the distribution of offsets without correcting for any global offset introduced by a poor acquisition of the field. Even before correcting for this effect (that could be eliminated by using a more elaborated acquisition procedure), the offsets are typically (68% of the cases) below half of the size of the central spaxel of each seven-spaxel MOS minibundle (the outlined hexagons represent one spaxel and the dashed circles represent the areas encompassing 68-95-99.7% of the centroids; see bottom panel). When we correct all coordinates by an average global offset (right panel) we find that with a precise acquisition and guiding we can have virtually all sources observed with errors below 0.2 arcsec (68% below 0.1 arcsec).

The throughput of the optical components being part of the FC-F unit of MEGARA (including the microlens arrays of LCB –plus 8 sky bundles– and the 92 MOS positioners and also the 44.5 m-long fiber links) was computed simultaneously with the that of the spectrograph main optics, VPHs and detector as part of the derivation of the MEGARA system sensitivity curves (see Figure 5).

### 3.2. Spectrograph performance

The tests carried out to evaluate the performance of the MEGARA spectrograph were based on observations in multiple setups of both ThAr and ThNe arc calibration lamps, spectrophotometric standard stars (including the white dwarf BD+33 2642 with a compact PNe around it), several nearby galaxies (NGC 7025, UGC 10205, NGC 7469, for LCB testing), and two Galactic Globular Clusters (M 15 and M 71, for MOS testing). In this subsection we focus on our results regarding the spectral resolution and efficiency performance of the instrument, while the results of the commissioning observations of BD+33 2642 and M 15 are described in Section 4. For the results on NGC 7025, UGC 10205 and NGC 7469 the reader is referred to Dullo et al. (2019), Catalán-Torrecilla et al. (2020) and Cazzoli et al. (2020), respectively.

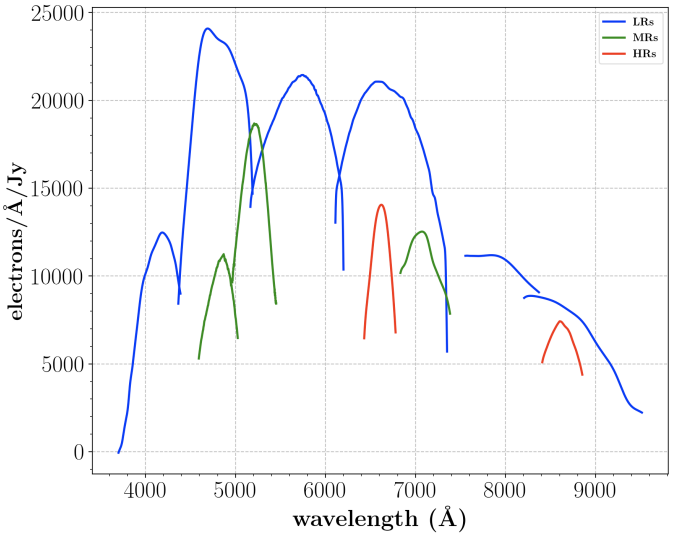


**Fig. 5.** System sensitivity curves of MEGARA in electrons per Å and per Jy (therefore, per second) of incoming flux at the corresponding wavelength. These curves represent the efficiency of the entire system at the different wavelengths and VPHs, including telescope, fore-optics, fibers, spectrograph main optics and VPHs, and the CCD detector. The curves shown correspond to the 6 LR, 10 MR and 2 HR VPHs listed in Table 2.

Once the instrument was integrated we first evaluated the degree of alignment of the two pseudo-slits with the collimator entrance by maximizing the flux from the fibers on the detector while observing the emission from halogen lamps in the FC-F Instrument Calibration Module (ICM hereafter). The fall in flux at both sides of these pseudo-slit positions was symmetric, which ensures that the positions inferred were indeed optimal. The same operation was performed to determine the optimal *closed*, *open-blue* and *open-red* positions of the instrument rotating shutter.

Based on the observation of ThAr arc-lamp calibration frames with the LR-I VPH, the repeatability of the pseudo-slit mechanism in pseudo-slit (focus) position was found to be better than 1.2 $\mu$m (2.4 $\mu$m) at the entrance focal plane or 0.04 pixels (0.08 pixels) on the detector. Given the large number of pupil elements of MEGARA (18 in total but 11 mounted simultaneously on the VPH wheel), the exchange between pupil elements is a very common operation for which we prioritize precision and, especially, repeatability. In the tests carried out during the daytime commissioning using LR-R ThNe arc lamps we inferred a repeatibility in the position of the fiber spectra after removing the VPH from the spectrograph pupil, rotating the wheel and putting it back to the pupil (but without manually removing the VPH from the wheel) of less than 0.07 pixels on the detector.

Although the MEGARA spectrograph has an athermal optomechanical design, which fulfills the image quality requirements once the optimal focus is set for each specific VPH and operating temperature, some vertical displacements (along the pseudo-slit) were observed as a function of temperature. This offset was found to change in an approximately linear fashion with temperature with a slope lower than 1 detector pixel (15 $\mu$m) per degree. Since the instrument is not temperature stabilized at the telescope, the acquisition of halogen-lamp flats at a similar temperature as the science frames is therefore advisable. The `megaradrp` (Pascual et al. 2018, 2019) allows for offsets to be applied to previously computed traces. Potential offsets are currently estimated manually but in the near future they will be ob-

tained automatically by cross-correlation or analytically based on the temperature difference between the scientific frame of interest and the halogen-lamp flat used for tracing measured by the MEGARA temperature sensor located near the position of the pseudo-slit. No offsets were identified in the dispersion direction of the detector throughout the entire range of temperatures experienced during the MEGARA commissioning period (see below).

The acquisition of images during this commissioning period using the ThNe and ThAr lamps provided by the FC-F ICM allowed us to derive the spectral resolution and wavelength ranges accessible to each LCB and MOS fiber through the 18 MEGARA VPHs. For all LR VPHs (except LR-Z) and all MR VPHs below 600 nm (MR-V and below) we used the optimal ThAr lamp. For the redder MRs, HR-R, HR-I and LR-Z VPHs we used ThNe instead (`megaradrp`-ready line catalogs for all setups are available at Cardiel & Pascual 2018). The resolving power versus wavelength coverage for each fiber and VPH are given in Figure 2 (gray lines). The mean of all 623 (644) fibers of the LCB (MOS) pseudo-slit are shown as thick black lines. The think black lines represent the corresponding mean$\pm 1\,\sigma$ curves. The thick colored lines represent the R vs. $\lambda$ design values associated to our image-quality requirement ($EED_{80} \leq 4$ pixels). Except for the slightly bluer wavelength coverage of HR-R, the rest of the VPHs match or surpass the instrument requirements. The fact that the actual image quality gets progressively better than the requirement the higher is the spectral resolution means that the overall image quality is set by the wavelength span to be focused simultaneously. During the commissioning we completed focus sequences at two temperatures, 11°C and 21°C, for all VPHs. The pseudo-slit was placed closest to the collimator at bluest wavelengths and lowest temperatures while we obtained slopes for the focus (roughly linear) variation of $0.7\,\mu$m Å$^{-1}$ and $40\,\mu$m/°, respectively for wavelength and temperature variations.

Although the reciprocal linear dispersion is not constant through the entire wavelength range of a given VPH, the `megaradrp` processes yields reduced data with the fixed reciprocal linear dispersion values given in column (10) of Table 2.

The observation of a number of spectrophotometric standard stars allowed us to derive sensitivity curves for all 18 MEGARA VPHs. In order to ensure that all the light from the standards was captured we used the LCB mode for this purpose. Since the fibers used in the MOS mode are identical in terms of the material, shape and size, these sensitivity curves are also used for the MOS observations in the corresponding VPH. In Figure 4 we show the sensitivity curves in units of electrons (or digital number) within an Å per Jy (i.e. per second). These curves represent the sensitivity of the entire system, telescope plus instrument, including the spectrograph main optics, the VPHs along with their flat windows (and also prisms in the case of the MR and HR VPHs), and the detector.

## 4. On-sky commissioning observations

The MEGARA nighttime commissioning period lasted for three runs, from June 24$^{\rm th}$ (night of first light) to July 3$^{\rm rd}$, July 24$^{\rm th}$ to August 2$^{\rm nd}$ and August 22$^{\rm nd}$ to August 31$^{\rm st}$ 2017. Our first light target was the White Dwarf BD+33 2642, a HST spectrophotometric standard star with spectral types in the literature ranging O7p D (Klemola 1962) and B2 IVp (Iriarte 1958) and FK5 equatorial coordinates $RA_{J2000}$=15$^{\rm h}$ 51$^{\rm m}$ 59$^{\rm s}$.885 and $Dec_{J2000}$=+32° 56' 54".33. This object was selected first because of (1) its nature of spectrophotometric standard with intermediate resolution spectra available in CALSPEC (Bohlin et al. 2014), so it could be used for calibration purposes, and (2) the fact that this object has been shown to host a extended but relatively faint ionized-gas nebula (PN G052.7+50.7) that fits the FoV of the MEGARA LCB (Napiwotzki et al. 1994), so it could be used to test the 2D spectroscopy capabilities of the instrument for the detection narrow emission lines in multiple spectral setups even beyond the goals of a first-light observation.

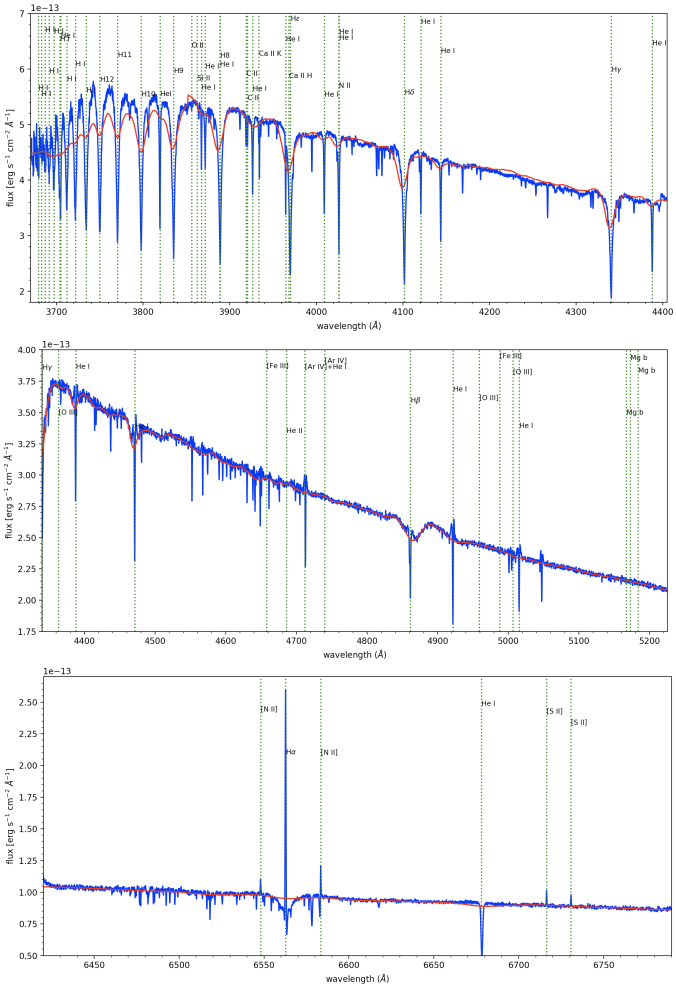


**Fig. 6.** MEGARA spectrum of the central 37 spaxels around spectrophotometric standard star BD+33 2642 obtained through the LR-U (top), LR-B (central) and HR-R (bottom) VPHs. The blue solid line shows the MEGARA spectrum, while the red line is the tabulated CALSPEC spectrum (Bohlin et al. 2014). The positions of some absorption (and in some cases also emission) lines are marked with green vertical dashed lines.

### 4.1. BD+33 2642 star and nebula

Although BD+33 2642 was observed through all 18 MEGARA VPH setups, we will show here only the results for the observation in two LR VPH (LR-U and LR-B; R~6 000) and one HR VPH (HR-R; R~20 000) that were all acquired on the night of June 26$^{\rm th}$ 2017, two nights after the first light, with total exposure times of 360, 180 and 360 seconds, respectively. These observations were processed with the `megaradrp` using halogen-lamps flats and ThAr & ThNe arc-lamp spectra taken during the nighttime commissioning period. The noise (rms) of the wavelength calibration obtained was below 0.04 Å for all fibers in the case of the LR VPHs and below 0.01 Å for the HR-R setup.

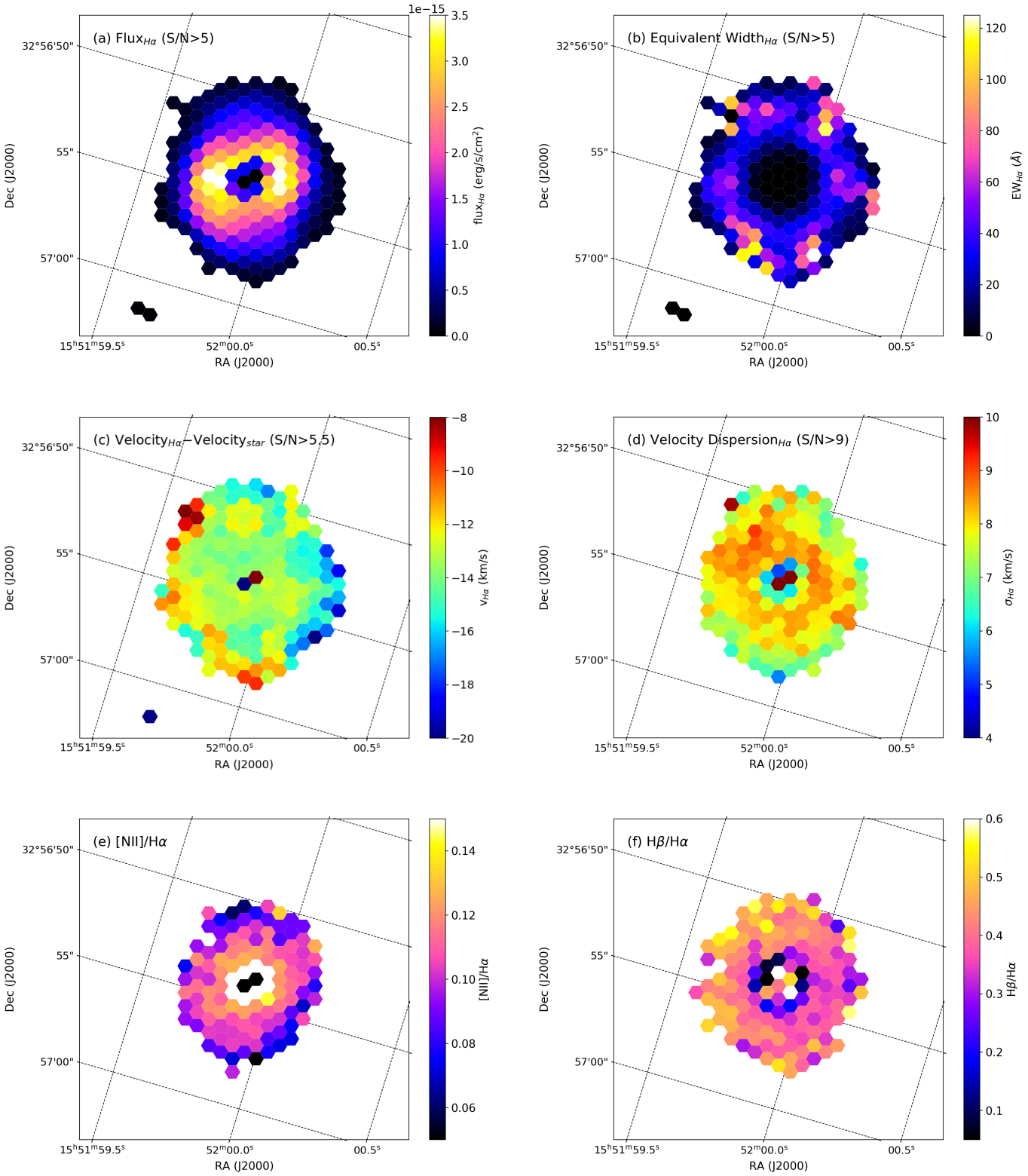


**Fig. 7.** Maps of the spatial distribution of line emission properties of PN G052.7+50.7 (nebula around BD+33 2642): **(a)** H$\alpha$ line flux of spaxels with signal-to-noise ratio at the peak of the line S/N>5. The flux is derived from the best-fitting Gauss-Hermite polynomials to the line profile after removing the adjacent continuum (van der Marel & Franx 1993). **(b)** H$\alpha$ equivalent width with S/N>5. **(c)** Radial velocity from H$\alpha$ relative to the velocity of the star BD+33 2642 (see text). **(d)** Velocity dispersion ($\sigma$ or h2) corrected for the HR-R VPH instrumental resolution. **(e)** [NII]$\lambda$6584Å/H$\alpha$ line ratio. Only spaxels with peak S/N>5 in [NII]$\lambda$6584Å are shown. **f)** H$\beta$/H$\alpha$ line ratio for spaxels with S/N> in H$\beta$.

In Figure 6 we show the LR-U (top), LR-B (central) and HR-R (bottom) spectra of BD+33 2642 extracted from the processed RSS frames by adding up a total of 37 LCB spaxels (three rings) around the spaxel where the centroid of the source is located for

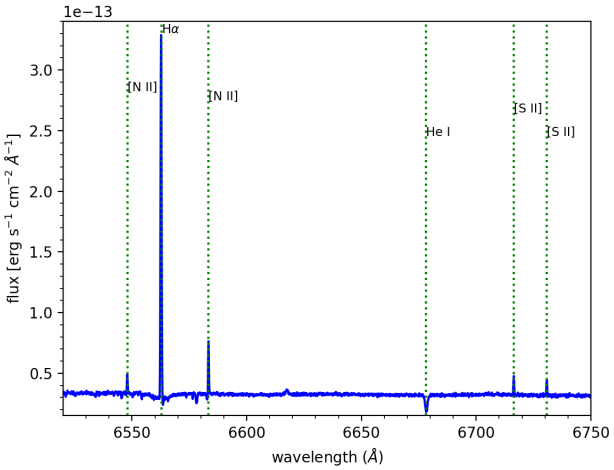


**Fig. 8.** HR-R spectrum of the PN G052.7+50.7 nebula obtained by adding up all spaxels with peak S/N>5 in [NII]$\lambda$6784Å but after excluding the 17 spaxels around the central star BD+33 2642. Note that despite excluding the central ∼2.5 arcsec the spectrum still shows stellar continuum and some absorption lines, including HeI$\lambda$6678.1Å.

each of the three spectral setups analyzed. This figure also includes the tabulated CALSPEC spectrum of BD+33 2642 and the position of a number of spectral features of interest. We emphasize here that the aperture used does not include all the line emission from the ionized-gas nebula surrounding BD+33 2642, also called PN G052.7+50.7 (see below).

Using the LR-B and HR-R RSS frames we then derived the spatial distribution and line profiles (including high-order moments) of emission lines arising from the nebula surrounding BD+23 2642. The line maps analyzed were those of H$\alpha$, H$\beta$ and [NII]$\lambda$6584Å along with the [NII]$\lambda$6584Å/H$\alpha$ and H$\beta$/H$\alpha$ line ratios. The results of this analysis are shown in Figure 7.

Panel (a) of Figure 7 shows the H$\alpha$ line flux of those spaxels with H$\alpha$ emission above S/N>5 at the peak of the line. They cover a nearly circular region (albeit a bit elongated along PA∼30°, measured from North to East) of ∼10 arcsec in diameter, i.e. twice the extension detected by Napiwotzki et al. (1994) using long-slit spectroscopy. Besides, the distribution is not perfectly symmetric since the H$\alpha$ emission is enhanced along PA∼ −70° (horizontally in Figure 7). Panel (b) shows that the H$\alpha$ equivalent width ranges between almost null in the center, where the continuum from the central star dominates (see Figure 6), to 40-60 Å in the surrounding nebula. The radial velocities shown in panel (c) are computed relative to that of the central star. In order to minimize errors we used the well isolated HeI$\lambda$6678.1Å absorption line (see Figure 6) in the same HR-R RSS used for the ionized-gas kinematics. Similar radial velocities were obtained when using the also relatively deep and well isolated CII$\lambda$6578.05Å line. Both lines are typical of B2-type giant stars.

All spaxels with H$\alpha$ emission are blue-shifted, with most of the inner nebular showing a relative velocity to the central star of −14 km s$^{-1}$. Most of this overall blue-shift can be explained by the relative orbital motion of BD+33 2642 with respect to the nebula that was found by Van Winckel et al. (2014) since at the date of our observations (JD=2457931.45139) the star was near its radial velocity maximum. Besides, we find a previously unreported bipolar structure with velocities ±6 km s$^{-1}$ around this value that is also coarsely aligned with the direction where the enhancement in H$\alpha$ flux emission is found.

The large distance provided by Gaia-DR2 (∼6.0±1.7 kpc vs. 3.3 kpc in Napiwotzki et al. 1994) confirms the nature of PN G052.7+50.7 as a halo post-AGB object and yields a physical radius for the emission nebula of 0.15 pc. The velocity structure of the nebula described above complicates the determination of its dynamical timescale. However, since the 14 km s$^{-1}$ blue-shift is mainly due to the orbital motion of BD+33 2642 and the time-averaged velocity of the star matches that of the inner nebula within 2-3 km s$^{-1}$ (Van Winckel et al. 2014), the ±6 km s$^{-1}$ bipolar kinematic structure seen at the edges of the nebula is the only evidence of its expansion. This value, given the 0.15 pc of radius of the nebula, yields a timescale of 25,000 yr, i.e. ten times larger than the value derived by Napiwotzki et al. (1994). On the other hand, the evolutionary timescale out of the AGB derived by these authors based on the best-fitting $T_{\rm eff}$ and $g$ to the star's spectrum is $6\,000^{+4000}_{-2000}$ K. In order to reconcile these numbers one possibility is that the observed bipolar expansion is lowered due to projection effects, so 25,000 yr would be an upper limit to the actual dynamical timescale. Alternatively, the extension of the emission nebula detected with MEGARA could be simply tracing the edge of the ionizing front, which is expected to move at a pace of ∼25 km s$^{-1}$ for this type os stars (Goldsworthy 1958). Such speed would yield a timescale of 6 000 yr for the nebula, perfectly matching the best estimate of the star's post-AGB evolution timescale.

The slow radial motions measured also result in low velocity dispersions within the nebula (see panel (d)), with values ranging between 6-9 km s$^{-1}$, once corrected for instrumental resolution ($\sigma_{\rm HR-R}$=6 km s$^{-1}$). We also find a gradient in velocity dispersion, with values close to 9 km s$^{-1}$ in the inner nebula decreasing to 6-7 km s$^{-1}$ in the outskirts. Although part of the line broadening and the observed gradient might be due to large-scale motions of gas within the nebula, these values are already compatible with thermal broadening for electron temperatures below $10^4$ K, as those inferred from the modeling of the physical conditions in the nebula by Napiwotzki et al. (1994).

The use of MEGARA@GTC has allowed us to determine also [NII]$\lambda$6784Å/H$\alpha$, H$\beta$/H$\alpha$ [SII]$\lambda\lambda$6717,6731ÅÅ/H$\alpha$ and [SII]$\lambda$6717Å/[SII]$\lambda$6731Å line ratios in this nebula, many of them for the first time. For the [NII]$\lambda$6784Å/H$\alpha$ and H$\beta$/H$\alpha$ line ratios the signal is enough to provide a map of all the spaxels with peak S/N>5 in both lines involved. These maps range between 0.08-0.13 for [NII]$\lambda$6784Å/H$\alpha$ (panel (e)) and 0.25-0.50 for H$\beta$/H$\alpha$ (panel (f)). For the rest of the line ratios we derived global values using a spectrum that is the result of adding up all spaxels with S/N>5 in [NII]$\lambda$6784Å but excluding the 17 spaxels around the central star. The resulting MEGARA HR-R spectrum is shown in Figure 8. The [SII]$\lambda\lambda$6717,6731ÅÅ/H$\alpha$ and [SII]$\lambda$6717Å/[SII]$\lambda$6731Å line ratios measured are 0.071±0.004 and 1.245±0.006, respectively. From the same HR-R spectrum we obtained [NII]$\lambda$6784Å/H$\alpha$=0.112±0.003 while using the same spaxels in both the LR-B and HR-R RSS frames we derived H$\beta$/H$\alpha$=0.39±0.02. Line flux errors were obtained as in Tresse et al. (1999) (see their Section 2.2).

### 4.2. M15 Globular Cluster

In order to test the performance of the MEGARA MOS robotic positioners (see Section 2.1) and the spectral performance of the instrument in the this mode we observed a number of bright stars (mostly RGB/AGB and HB stars) in the Galactic Globular clus-

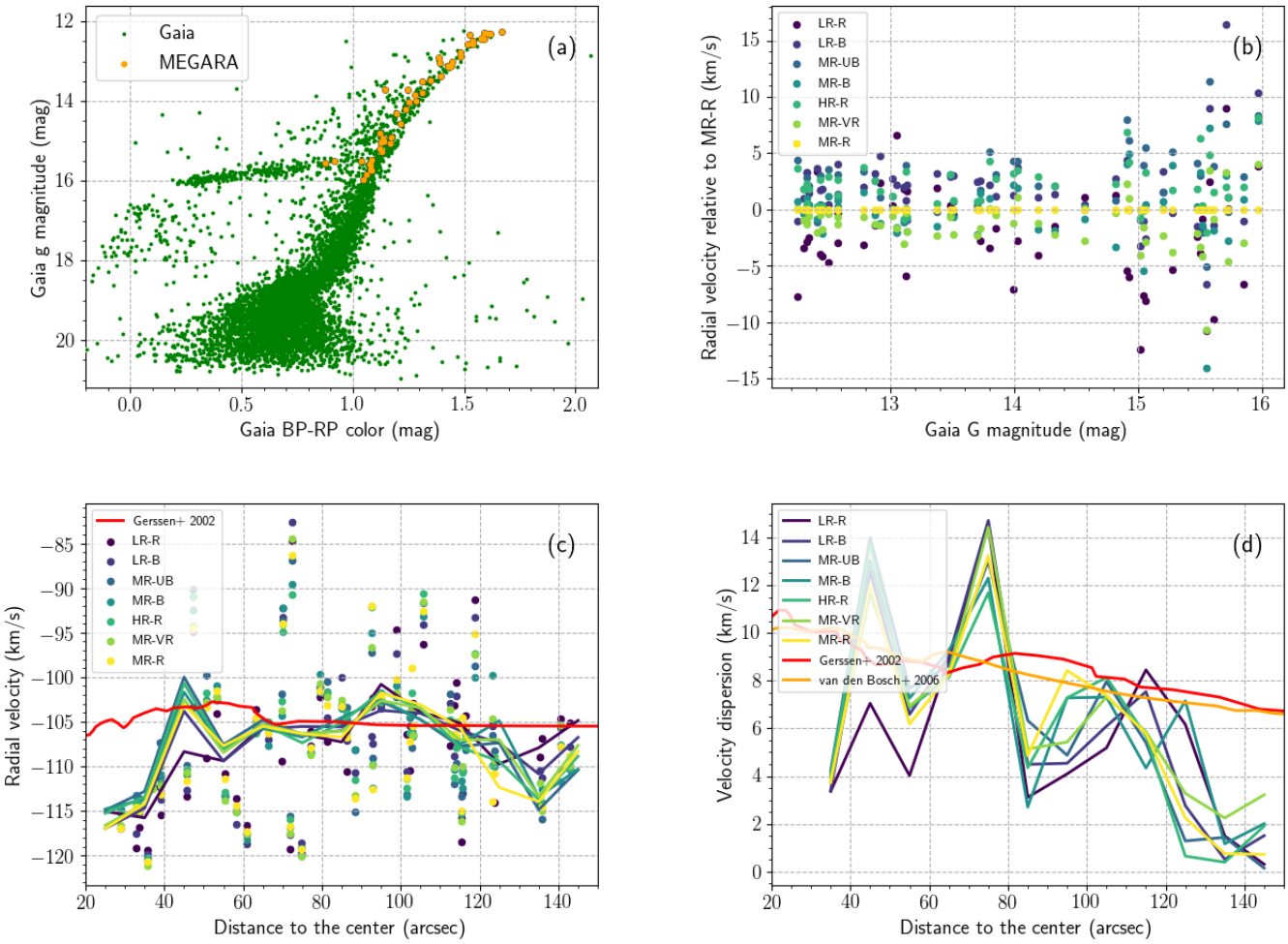


**Fig. 9.** Kinematic analysis of the MEGARA MOS observations of M 15. **(a)** Color-magnitude diagram of M 15 stars identified in Gaia DR2 (green points) and those 49 stars observed with MEGARA as part of its commissioning observations having a Gaia counterpart (orange points). **(b)** Dispersion of the radial velocity measurements of the 49 stars in the seven spectral setups analyzed relative to those measured with the R∼12 000 MR-R VPH. **(c)** Individual and 10 arcsec binned measurements of the line-of-sight velocity as a function of Clustercentric distance in arcsec. As in panel (b) the points a color-coded by VPH. The same color is used for the data points and for the lines with the binned measurements. The rotation curve from Gerssen et al. (2002) is shown as a solid red line. **(d)** The same as for (c) but for the line-of-sight velocity dispersion. In this case, in addition to the $\sigma$ curve Gerssen et al. (2002) we also include the curve from van den Bosch et al. (2006).

ter M 15 with cluster-centric distances ranging between 25 to 145 arcsec. M 15 was observed in the MOS mode in all 18 VPHs. The results presented here correspond to the observations in the LR-B, LR-R, MR-UB, MR-B, MR-VR, MR-R and HR-R setups. In Table 3 we show the observing dates, exposure times and average airmasses of all seven spectral setups. We used a common MOS configuration for LR-B, LR-R, MR-UB, MR-B and HR-R and another one for the MR-VR and MR-R setups. Out of the 92 robotic positioners, four were set inactive during the commissioning observations while the rest were available to be positioned on M15 stars. We analyze here the results of the properties of 49 stars in M 15 matching the positions of objects in Gaia DR2 catalog (Gaia Collaboration et al. 2016, 2018) that were undoubtedly part of either Horizontal Branch (HB) or the Red-Giant Branch (RGB; note that AGB stars could be also present) of the cluster (see panel (a) of Figure 9). The membership of the M 15 Gaia DR2 stars was assigned based on the following criteria:

$322.293^\circ < \mathrm{RA}_{\mathrm{J2000}} < 322.683^\circ$

$11.976^\circ < \mathrm{DEC}_{\mathrm{J2000}} < 12.359^\circ$

$-1.5\,\mathrm{mas} < \pi < 1.5\,\mathrm{mas}$

$-1.93\,\mathrm{mas\,yr^{-1}} < \mathrm{pm\ RA}_{\mathrm{J2000}} < 0.68\,\mathrm{mas\,yr^{-1}}$

$-2.05\,\mathrm{mas\,yr^{-1}} < \mathrm{pm\ DEC}_{\mathrm{J2000}} < -5.5\,\mathrm{mas\,yr^{-1}}$

Once the MOS spectra were processed using the `megaradrp`, we obtained the stars' radial velocities using iSpec by cross correlation with spectral templates (Blanco-Cuaresma et al. 2014). Out of the 49 M 15 stars analyzed, seven had also radial velocities measured in Gaia DR2. The setup yielding the smallest for these stars in common with Gaia in terms of radial velocity was MR-R, where a mean difference of 1.2 km s$^{-1}$ and a standard deviation of 2.9 km s$^{-1}$ were obtained. The difference in radial velocity between the average of the 49 stars in MR-R and each of all other six setups was applied in order to put all measurements in the same system, which, as mentioned above, is also the closest to the Gaia DR2 barycentric velocity measurements.

**Table 3.** Summary of observations of M15 presented in this paper.

| VPH (1) | Date (2) | $t_{exp}$ (s) (3) | am (4) | Arc (5) | Config. (6) |
|---|---|---|---|---|---|
| LR-B | 2017/07/31 | 3×300 | 1.46 | ThAr | 796f63f0 |
| LR-R | 2017/07/31 | 3×600 | 1.05 | ThNe | 796f63f0 |
| MR-UB | 2017/08/23 | 3×1200 | 1.05 | ThAr | 796f63f0 |
| MR-B | 2017/08/23 | 3×600 | 1.12 | ThAr | 796f63f0 |
| MR-VR | 2017/08/24 | 3×900 | 1.14 | ThNe | 0859ebf3 |
| MR-R | 2017/08/26 | 3×600 | 1.39 | ThNe | 0859ebf3 |
| HR-R | 2017/08/23 | 3×600 | 1.32 | ThNe | 796f63f0 |

**Notes.** Column 1: VPH setup. Column 2: Observing night. Column 3: Number of images acquired and exposure time per image in seconds. Column 4: Airmass for the middle image. Column 5: Arc lamp used for wavelength calibration. Column 6: Fiber MOS configuration (this represents part of the unique UUID used for each configuration of the robotic positioners).

In panel (b) of Figure 9 we show the differences between the radial velocity (once corrected for the global offsets described above) of the stars in each setup and that defined as closest reference to Gaia DR2 (MR-R). The standard deviation of our measurements are ±2-3 $km^{-1}$ for all magnitudes. We then binned the stars by Clustercentric distance in bins of 10 arcsec to determine the average velocity and velocity dispersion (as in Gerssen et al. 2002) radial profiles. The central position adopted for M 15 was the one published by Goldsbury et al. (2010). Panel (c) shows both the individual radial velocity measurements and the resulting binned radial velocity profiles for all seven spectral setups used in this paper. These curves agree within the rms of the individual measurements (panel (b)). The rotation curve derived by Gerssen et al. (2002) is shown as red solid line. The difference in radial velocity is likely due to the use of only a 49 stars in this work compared to the hundreds of stars at the same radial range used in Gerssen et al. (2002), that were mainly taken from Gebhardt et al. (2000). Finally, in panel (d) we show the radial variation of the line-of-sight velocity dispersion ($\sigma$) with the Clustercentric distance for all seven VPHs analyzed along with those obtained by Gerssen et al. (2002) (in red) and van den Bosch et al. (2006) (in orange).

Although only one MOS pointing was acquired during the MEGARA commissioning, the results presented here already show that the instrument can be effectively used to determine stellar kinematics with a radial velocity precision of the order or 2-3 km $s^{-1}$ in $g$~16 mag stars at distances of ~6 kpc in about 30 minutes worth of observing time.

## 5. Conclusions

In this paper we have presented the results of the commissioning of the MEGARA instrument at the Gran Telescopio Canarias in both its two observing modes, the LCB IFU and the MOS, in all 18 spectral setups (6 LR, 10 MR and 2 HR VPHs) that took place during the Spring-Summer of 2017. The analysis of both the daytime and nighttime commissioning of MEGARA have showed that the instrument fulfills all its design requirements and that since it being offered to the community in July 2018 is ready to produce science using a unique combination of versatility (IFU & MOS), efficiency, spectral resolution (R=6 000-20 000) and wavelength coverage (365-970 nm).

The on-sky commissioning observations of BD+33 2642 with the MEGARA LCB IFU and M 15 with the MEGARA MOS and the results derived from these highlight some of the unique but, at the same time, distinct applications of this instrument. Other results coming out of MEGARA are described in Dullo et al. (2019), Catalán-Torrecilla et al. (2020), Cazzoli et al. (2020) and García-Vargas et al. (2020).

*Acknowledgements.* We acknowledge financial support from the Spanish Ministry of Economy and Competitiveness (MINECO) under grant numbers AYA2016-75808-R and RTI2018-096188-B-I00, which are partly funded by the European Regional Development Fund (ERDF), from the Excellence Network *"Red para la explotación científica de MEGARA@GTC en España"* with code AYA2017-90589-REDT, and from the Comunidad de Madrid Tec2Space project S2018/NMT-4291. Based on observations made with the Gran Telescopio Canarias (GTC), installed at the Spanish Observatorio del Roque de los Muchachos of the Instituto de Astrofísica de Canarias, in the island of La Palma. This work has made use of data from the European Space Agency (ESA) mission *Gaia* (`https://www.cosmos.esa.int/gaia`), processed by the *Gaia* Data Processing and Analysis Consortium (DPAC, `https://www.cosmos.esa.int/web/gaia/dpac/consortium`). Funding for the DPAC has been provided by national institutions, in particular the institutions participating in the *Gaia* Multilateral Agreement.

## References

Bacon, R., Accardo, M., Adjali, L., et al. 2010, in Proc. SPIE, Vol. 7735, Ground-based and Airborne Instrumentation for Astronomy III, 773508
Bacon, R., Copin, Y., Monnet, G., et al. 2001, MNRAS, 326, 23
Blanco-Cuaresma, S., Soubiran, C., Heiter, U., & Jofré, P. 2014, iSpec: Stellar atmospheric parameters and chemical abundances
Bohlin, R. C., Gordon, K. D., & Tremblay, P. E. 2014, PASP, 126, 711
Cardiel, N. & Pascual, S. 2018, guaix-ucm/megaradrp-calibrations: Release 2018.1
Carrasco, E., Páez, G., Izazaga, R., et al. 2016, in Proc. SPIE, Vol. 9908, Ground-based and Airborne Instrumentation for Astronomy VI, 990885
Castillo-Domínguez, E., Ferrusca, D., Tulloch, S., et al. 2012, in Proc. SPIE, Vol. 8446, Ground-based and Airborne Instrumentation for Astronomy IV, 84465Y
Castillo-Morales, A., Eliche-Moral, M. C., Pascual, S., et al. 2013, in Revista Mexicana de Astronomia y Astrofisica, vol. 27, Vol. 42, Revista Mexicana de Astronomia y Astrofisica Conference Series, 123–123
Castillo-Morales, Á., Pascual, S., & Gil de Paz, A. 2018, MEGARA Data Reduction Cookbook
Catalán-Torrecilla, C., Castillo-Morales, Á., Gil de Paz, A., et al. 2020, ApJ, 890, 5
Cazzoli, S., Gil de Paz, A., Márquez, I., et al. 2020, MNRAS[arXiv:2002.04031]
Cepa, J., Aguiar-Gonzalez, M., Bland-Hawthorn, J., et al. 2003, in Proc. SPIE, Vol. 4841, Instrument Design and Performance for Optical/Infrared Ground-based Telescopes, ed. M. Iye & A. F. M. Moorwood, 1739–1749
Dalton, G., Trager, S., Abrams, D. C., et al. 2018, in Society of Photo-Optical Instrumentation Engineers (SPIE) Conference Series, Vol. 10702, Ground-based and Airborne Instrumentation for Astronomy VII, 107021B
Dullo, B. T., Chamorro-Cazorla, M., Gil de Paz, A., et al. 2019, ApJ, 871, 9
Ferrusca, D., Castillo-Domínguez, E., Velázquez, M., et al. 2014, in Proc. SPIE, Vol. 9147, Ground-based and Airborne Instrumentation for Astronomy V, 91476S
Gaia Collaboration, Brown, A. G. A., Vallenari, A., et al. 2018, A&A, 616, A1
Gaia Collaboration, Prusti, T., de Bruijne, J. H. J., et al. 2016, A&A, 595, A1
García-Vargas, M. L., Carrasco, E., Mollá, M., et al. 2020, Monthly Notices of the Royal Astronomical Society, 493, 871
Garzón, F., Castro, N., Insausti, M., et al. 2016, in Proc. SPIE, Vol. 9908, Ground-based and Airborne Instrumentation for Astronomy VI, 99081J
Gebhardt, K., Pryor, C., O'Connell, R. D., Williams, T. B., & Hesser, J. E. 2000, AJ, 119, 1268
Gerssen, J., van der Marel, R. P., Gebhardt, K., et al. 2002, AJ, 124, 3270
Goldsbury, R., Richer, H. B., Anderson, J., et al. 2010, AJ, 140, 1830
Goldsworthy, F. A. 1958, Reviews of Modern Physics, 30, 1062
Hammer, F., Hill, V., & Cayatte, V. 1999, Journal des Astronomes Francais, 60, 19
Hammer, F., Morris, S., Kaper, L., et al. 2016, in Proc. SPIE, Vol. 9908, Ground-based and Airborne Instrumentation for Astronomy VI, 990824
Iriarte, B. 1958, ApJ, 127, 507
Izazaga, R., Carrasco, E., Aguirre, D., et al. 2016, in Proc. SPIE, Vol. 9912, Advances in Optical and Mechanical Technologies for Telescopes and Instrumentation II, 99120D
Klemola, A. R. 1962, AJ, 67, 740

Martínez-Delgado, I., Sánchez-Blanco, E., Pérez-Calpena, A., et al. 2016, in Proc. SPIE, Vol. 9912, Advances in Optical and Mechanical Technologies for Telescopes and Instrumentation II, 99124D
Mayor, M., Pepe, F., Queloz, D., et al. 2003, The Messenger, 114, 20
Napiwotzki, R., Heber, U., & Koeppen, J. 1994, A&A, 292, 239
Pascual, S., Cardiel, N., Gil de Paz, A., et al. 2019, in Highlights on Spanish Astrophysics X, Proceedings of the XIII Scientific Meeting of the Spanish Astronomical Society held on July 16-20, 2018, in Salamanca, Spain, ISBN 978-84-09-09331-1. B. Montesinos, A. Asensio Ramos, F. Buitrago, R. Schödel, E. Villaver, S. Pérez-Hoyos, I. Ordóñez-Etxeberria (eds.) p. 227-227, ed. B. Montesinos, A. Asensio Ramos, F. Buitrago, R. Schödel, E. Villaver, S. Pérez-Hoyos, & I. Ordóñez-Etxeberria, 227–227
Pascual, S., Cardiel, N., Picazo-Sanchez, P., Castillo-Morales, A., & de Paz, A. G. 2018
Pasquini, L., Avila, G., Blecha, A., et al. 2002, The Messenger, 110, 1
Pérez-Calpena, A., Arrillaga, X., Gil de Paz, A., et al. 2012, in Proc. SPIE, Vol. 8446, Ground-based and Airborne Instrumentation for Astronomy IV, 84465E
Pérez-Calpena, A., García-Vargas, M. L., Arrillaga, X., et al. 2014, in Proc. SPIE, Vol. 9147, Ground-based and Airborne Instrumentation for Astronomy V, 91475N
Pérez-Calpena, A., García-Vargas, M.-L. L., Gil de Paz, A., et al. 2018a, in Society of Photo-Optical Instrumentation Engineers (SPIE) Conference Series, Vol. 10705, Modeling, Systems Engineering, and Project Management for Astronomy VIII, 107050A
Pérez-Calpena, A., Sánchez-Blanco, E., Martínez-Delgado, I., et al. 2016, in Proc. SPIE, Vol. 9912, Advances in Optical and Mechanical Technologies for Telescopes and Instrumentation II, 99125L
Pérez-Calpena, A., Sánchez-Blanco Mancera, E., Gomez-Alvarez, P., et al. 2018b, in Society of Photo-Optical Instrumentation Engineers (SPIE) Conference Series, Vol. 10706, Proc. SPIE, 107062C
Reiss, R., Deiries, S., Lizon, J.-L., & Rupprecht, G. 2012, in Proc. SPIE, Vol. 8446, Ground-based and Airborne Instrumentation for Astronomy IV, 84462P
Sharp, R., Saunders, W., Smith, G., et al. 2006, in Proc. SPIE, Vol. 6269, Society of Photo-Optical Instrumentation Engineers (SPIE) Conference Series, 62690G
Telesco, C. M., Packham, C., Varosi, F., et al. 2013, in Revista Mexicana de Astronomia y Astrofisica, vol. 27, Vol. 42, Revista Mexicana de Astronomia y Astrofisica Conference Series, 81–83
Tresse, L., Maddox, S., Loveday, J., & Singleton, C. 1999, MNRAS, 310, 262
Tulloch, S., Gil de Paz, A., Gallego, J., Zamorano, J., & Tapia, C. 2012, in Proc. SPIE, Vol. 8453, High Energy, Optical, and Infrared Detectors for Astronomy V, 845328
Tulloch, S. M., García-Vargas, M. L., Maldonado, M., et al. 2013, in Revista Mexicana de Astronomia y Astrofisica, vol. 27, Vol. 42, Revista Mexicana de Astronomia y Astrofisica Conference Series, 126–126
van den Bosch, R., de Zeeuw, T., Gebhardt, K., Noyola, E., & van de Ven, G. 2006, ApJ, 641, 852
van der Marel, R. P. & Franx, M. 1993, ApJ, 407, 525
Van Winckel, H., Jorissen, A., Exter, K., et al. 2014, A&A, 563, L10
Zamorano, J., Gil de Paz, A., Gallego, J., et al. 2013, in Revista Mexicana de Astronomia y Astrofisica, vol. 27, Vol. 42, Revista Mexicana de Astronomia y Astrofisica Conference Series, 127–127

[1] Universidad Complutense de Madrid (UCM, Spain) and Instituto de Física de Partículas y del Cosmos (IPARCOS)
e-mail: agil@fis.ucm.es
[2] Instituto Nacional de Astrofísica, Óptica y Electrónica (INAOE, Mexico)
[3] Instituto de Astrofísica de Andalucía (IAA-CSIC, Spain)
[4] Universidad Politécnica de Madrid (UPM, Spain)
[5] FRACTAL S.L.N.E. (Spain)
[6] AVS S.L. (Spain)
[7] Centro de Investigaciones en Óptica (CIO, Mexico)
[8] Instituto de Astrofísica de Canarias (IAC, Spain)
[9] Centro de Astrobiología (INTA/CSIC, Spain)
[10] Observatoire de Genève, Université de Genève (Switzerland)
[11] Centro de Estudios de Física del Cosmos de Aragón (CEFCA, Spain)
[12] Department of Astronomy, University of Florida (USA)
[13] Universidad de Granada (Spain)
[14] CIEMAT (Spain)
[15] Department of Astronomy, University of Wisconsin at Madison (USA)
[16] Universidad Nacional Autónoma de México (IA-UNAM, Mexico)
[17] Department of Physics and Astronomy, University College London (UK)